

Evidence for the production of thermal muon pairs with masses above $1 \text{ GeV}/c^2$ in 158A GeV Indium-Indium collisions

NA60 Collaboration

R. Arnaldi¹¹, K. Banicz^{4,6}, K. Borer¹, J. Castor⁵, B. Chaurand⁹, W. Chen², C. Cicalò³, A. Colla¹¹, P. Cortese¹¹, S. Damjanovic^{4,6}, A. David^{4,7}, A. de Falco³, A. Devaux⁵, L. Ducroux⁸, H. En'yo¹⁰, J. Fargeix⁵, A. Ferretti¹¹, M. Floris³, A. Förster⁴, P. Force⁵, N. Guettet^{4,5}, A. Guichard⁸, H. Gulkanian¹², J.M. Heuser¹⁰, M. Keil^{4,7}, L. Kluberg⁹, Z. Li², C. Lourenço⁴, J. Lozano⁷, F. Manso⁵, P. Martins^{4,7}, A. Masoni³, A. Neves⁷, H. Ohnishi¹⁰, C. Oppedisano¹¹, P. Parracho^{4,7}, P. Pillot⁸, T. Poghosyan¹², G. Puddu³, E. Radermacher⁴, P. Ramalhete^{4,7}, P. Rosinsky⁴, E. Scomparin¹¹, J. Seixas⁷, S. Serci³, R. Shahoyan^{4,7} ^a, P. Sonderegger⁷, H.J. Specht⁶, R. Tieulent⁸, G. Usai³, R. Veenhof⁷, and H.K. Wöhri^{3,7}.

¹ Laboratory for High Energy Physics, Bern, Switzerland.

² BNL, Upton, New York, USA.

³ Università di Cagliari and INFN, Cagliari, Italy.

⁴ CERN, Geneva, Switzerland.

⁵ LPC, Université Blaise Pascal and CNRS-IN2P3, Clermont-Ferrand, France.

⁶ Physikalisches Institut der Universität Heidelberg, Germany.

⁷ IST-CFTP, Lisbon, Portugal.

⁸ IPN-Lyon, Univ. Claude Bernard Lyon-I and CNRS-IN2P3, Lyon, France.

⁹ LLR, Ecole Polytechnique and CNRS-IN2P3, Palaiseau, France.

¹⁰ RIKEN, Wako, Saitama, Japan.

¹¹ Università di Torino and INFN, Italy.

¹² YerPhI, Yerevan, Armenia.

Date: 11/12/2008

Abstract. The yield of muon pairs in the invariant mass region $1 < M < 2.5 \text{ GeV}/c^2$ produced in heavy-ion collisions significantly exceeds the sum of the two expected contributions, Drell-Yan dimuons and muon pairs from the decays of D meson pairs. These sources properly account for the dimuons produced in proton-nucleus collisions. In this paper, we show that dimuons are also produced in excess in 158 A GeV In-In collisions. We furthermore observe, by tagging the dimuon vertices, that this excess is not due to enhanced D meson production, but made of *prompt* muon pairs, as expected from a source of thermal dimuons specific to high-energy nucleus-nucleus collisions. The yield of this excess increases significantly from peripheral to central collisions, both with respect to the Drell-Yan yield and to the number of nucleons participating in the collisions. Furthermore, the transverse mass distributions of the excess dimuons are well described by an exponential function, with inverse slope values around 190 MeV. The values are independent of mass and significantly lower than those found at masses below $1 \text{ GeV}/c^2$, rising there up to 250 MeV due to radial flow. This suggests the emission source of thermal dimuons above $1 \text{ GeV}/c^2$ to be of largely partonic origin, when radial flow has not yet built up.

PACS. 14.40.Lb – 25.75.Nq – 25.75.Cj

1 Introduction

The intermediate mass region (IMR) of the dimuon mass spectrum, between the ϕ and the J/ψ resonances, is expected to be well suited to search for thermal dimuon production [1], due to the favourable relative production yield with respect to the other contributions (Drell-Yan dimuons, meson decays, etc).

Intermediate mass dimuon production in proton-nucleus and heavy-ion collisions was previously investigated by NA38 [2] and HELIOS-3 [3] in p-W and S-U(W) collisions at 200 GeV, and by NA50 [4,5] in p-A (where A stands for Al, Cu, Ag, W) and Pb-Pb collisions, respectively at 450 and 158 GeV. All three experiments reported a very reasonable description of the IMR opposite-sign dimuon mass continuum measured in the “elementary” proton-nucleus collisions. This continuum could be accounted for

^a Corresponding author: ruben.shahoyan@cern.ch

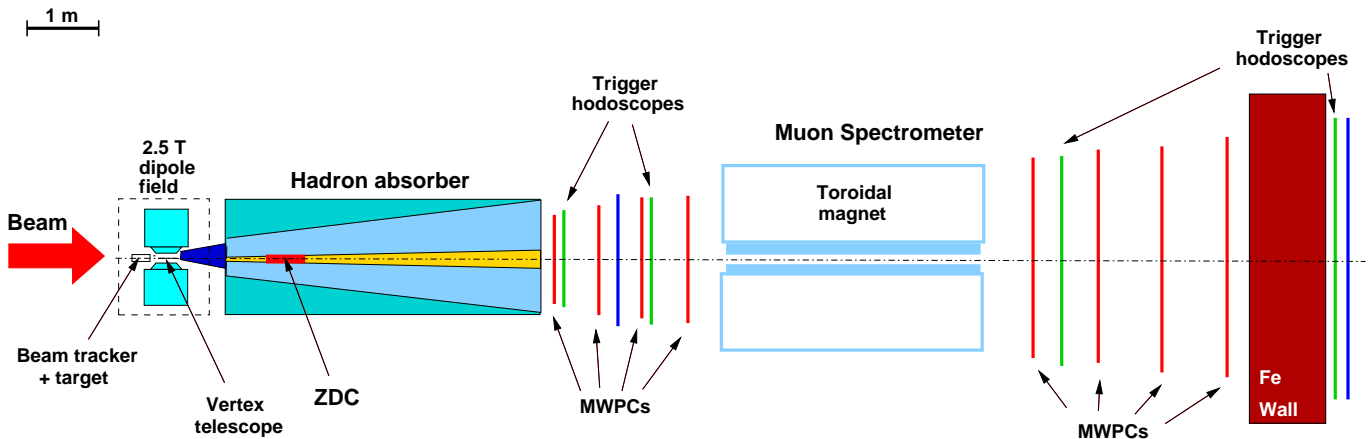


Fig. 1. Schematic representation of the NA60 experimental layout.

by a superposition of the two expected “signal” processes, the Drell-Yan dimuons and the muon pairs resulting from simultaneous semi-muonic decays of (correlated) D and \bar{D} mesons, on the top of a “background” contribution. The latter is due to uncorrelated decays of pions and kaons and can be estimated from the measured like-sign muon pairs. In contrast, all experiments observed that the opposite-sign dimuon samples collected in the heavy-ion collision systems, taking into account the estimated background contribution, significantly exceeded the level expected from Drell-Yan and “open charm” sources, calculated using the same procedures that successfully reproduced the p-A data.

As discussed in [6], two prime interpretations were able to describe the findings of NA38 and NA50 equally well: the long-sought thermal dimuons [7], and an increase in the open charm production cross section per nucleon, from p-A to A-A collisions [8]. Several other reasons which could increase the yield of IMR dimuons were also proposed. Alternatively to charm enhancement, the number of muon pairs entering the phase space window of the experiment could be increased, while the total charm production cross section remains unchanged. This could result from, *e.g.*, the smearing of the D/\bar{D} pair correlation resulting from rescattering of the charmed quarks or mesons in the surrounding dense matter [9]. It was also suggested that the mass spectrum of the Drell-Yan dimuons could be modified in heavy-ion collisions with respect to the proton-nucleus case, because of higher-twist effects that increase the yield of low mass dimuons [10]. Another source of dimuons that could be present in heavy-ion collisions, while being negligible in p-nucleus collisions, is secondary Drell-Yan production, where the quark-antiquark annihilation uses valence antiquarks from produced pions [11].

A decisive step in understanding the origin of the excess dimuons is to clarify the decade-long ambiguity between prompt dimuons and off-vertex muon pairs. In the first case they can be thermal dimuons or extra Drell-Yan dimuons; in the second case they result from decays of D mesons, which have a relatively long lifetime: $c\tau = 312 \mu\text{m}$ for the D^+ and $123 \mu\text{m}$ for the D^0 . The clarification of the

physical origin of the IMR dimuon excess was one of the main motivations of the NA60 experiment. Thanks to its ability to measure the *offset* of the muons with respect to the interaction vertex, NA60 can separate, on a statistical basis, the prompt dimuons from the off-vertex muon pairs.

In this paper we present a study of the intermediate mass dimuons produced in In-In collisions at 158 GeV/nucleon, based on data collected by the NA60 experiment in 2003. The paper is organized as follows: Section 2 describes the NA60 experimental setup, the data reconstruction procedure and the general performance of the apparatus; Section 3 explains in some detail the background subtraction procedure; Section 4 presents the results. Preliminary results were presented before [12].

2 The NA60 experimental setup and data reconstruction

Figure 1 shows a general view of the NA60 apparatus. Its main components are the muon spectrometer (MS), previously used by the NA38 and NA50 experiments [13], and a novel radiation-hard silicon pixel vertex tracker (VT) with high granularity and high readout speed [14], placed inside a 2.5 T dipole magnet just downstream of the targets (see Fig. 2). The first spectrometer is separated from the sec-

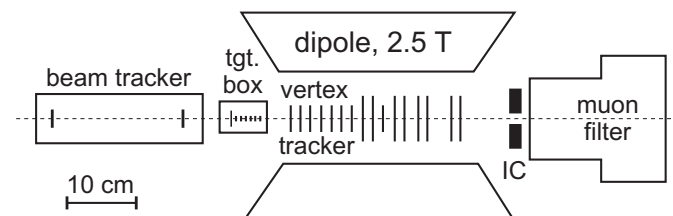


Fig. 2. View of the target region. From the left: 2 stations of the beam tracker followed by 7 Indium targets and 16 planes of the vertex tracker.

ond by a hadron absorber with a total effective thickness of $\sim 14 \lambda_{\text{int}}$ and $\sim 50 X_0$.

Before entering into more details, we list the key features of this somewhat unique setup:

- The vertex telescope tracks all charged particles *upstream* of the hadron absorber and determines their momenta independently of the MS, free from multiple scattering effects and energy loss fluctuations in the absorber. The matching of the muon tracks before and after the absorber, both in *coordinate and momentum space*, strongly improves the dimuon mass resolution in the low-mass region (less so higher up), significantly reduces the combinatorial background due to π and K decays and makes it possible to measure the muon offset with respect to the primary interaction vertex.
- The additional bend by the dipole field in the target region deflects muons with lower momenta into the acceptance of the MS, thereby strongly enhancing the opposite-sign dimuon acceptance, in particular at low masses and low transverse momenta, with respect to all previous dimuon experiments. A complete acceptance map in two-dimensional M - p_T space is contained in [15].
- The selective dimuon trigger and the radiation-hard vertex tracker with its high read-out speed allow the experiment to run at very high rates for extended periods, maintaining the original high luminosity of dimuon experiments despite the addition of an open spectrometer.

A detailed description of the muon spectrometer can be found in [13]. Its magnet defines the rapidity window where the dimuons are accepted, $3 < y_{\text{lab}} < 4$. The trigger system is based on four hodoscopes along the beam direction. Each of them has hexagonal symmetry, with the sextants operating independently. The system provides a highly selective dimuon trigger requiring that the four hodoscope slabs hit by each muon match one of the predefined patterns. This ensures that the muon was produced in the target region. In addition, the trigger imposes that the two muons must be detected in different sextants.

A detailed description of the radiation-hard silicon pixel vertex tracker used by NA60 in 2003 can be found in [16]. The readout pixel chips, developed for the ALICE and LHC-B experiments [17], operate with a 10 MHz clock frequency. The VT can provide up to 12 space points per track, 9 of them from planes oriented such that the horizontal coordinate (in the bending plane) is measured with higher precision.

The target system is composed of seven Indium sub-targets, 1.5 mm thick each and separated by an inter-distance of 8 mm, adding up to an interaction probability of 16% for the incident Indium ions. An interaction counter is located downstream of the VT. It is made of 2 scintillator blades, appropriately holed to let the beam pass through. They are independently read by 2 photo-multiplier tubes in coincidence and thus allow to tag the interactions in the target region. A beam tracker [18], made of two tracking stations 20 cm apart, was placed upstream of the target system. The beam tracker allows to measure the flight path of the incoming ions and to derive the transverse coordinates of the interaction point, in

the target, with an accuracy of 20 μm , independently of the collision centrality. A zero degree calorimeter, previously used in NA50, is located in the beam line, inside the muon filter, just upstream of the Uranium beam dump. It estimates the centrality of each nucleus-nucleus collision through the measurement of the energy deposited by the beam “spectator” nucleons.

Around 230 million dimuon triggers were recorded on tape during the 2003 run. In approximately half of these events a dimuon was reconstructed from the muon spectrometer data. Two data samples were collected, with different currents in the ACM toroidal magnet: 4000 A and 6500 A. The higher field reduces the acceptance in the highly populated region of low transverse mass (m_T) muon pairs, thereby increasing the number of high mass dimuon events collected per day, for a constant lifetime of the data acquisition system. The details of the event selection can be found in [16].

The reconstruction of the raw data proceeds in several steps. First, muon tracks are determined from the data of the eight MWPCs and validated by the hits recorded in the trigger hodoscopes. If the event has two reconstructed muon tracks which fulfil the trigger conditions, the tracks in the silicon planes of the vertex tracker are also reconstructed, and the interaction vertices are searched for. The track reconstruction efficiency is $\sim 95\%$ for peripheral In-In collisions and $\sim 90\%$ for the most central ones. The key step in the data reconstruction is the matching between the muon track, extrapolated from the muon spectrometer to the target region, and the charged tracks found in the vertex tracker. This is done by selecting those associations between the MS tracks and the VT tracks which give the smallest weighted squared distance (*matching* χ^2) between these two tracks, in the space of angles and inverse momenta, taking into account their error matrices. The matching procedure combines the good MS momentum resolution ($\sigma_p/p \sim 2\%$) with the excellent VT angular precision ($\simeq 1$ mrad) to obtain the kinematics of the muon before undergoing the multiple scattering and energy loss induced by the hadron absorber. This procedure, as mentioned before, improves the dimuon mass resolution, from 70-80 MeV/ c^2 to 20-25 MeV/ c^2 in the ω and ϕ mass region, and allows to correlate the muon’s trajectory with the interaction vertex, the point of primary interest for the present paper.

The resolution of the vertex determination, and its dependence on the number of tracks associated with the vertex, can be obtained from the dispersion between the measurements provided by the beam tracker and by the vertex tracker. As shown in Fig. 3, it is better than 10 μm in x and 15 μm in y , except for the most peripheral collisions.

Figure 4 shows the distribution of the z coordinate of the reconstructed vertices, for the events with only one vertex found. We can clearly identify the seven In targets, placed between the two windows that keep the target box in vacuum, downstream of the two beam tracker stations, also placed in vacuum.

The resolution of the offset distance measured between the matched muon tracks and the collision vertex can be

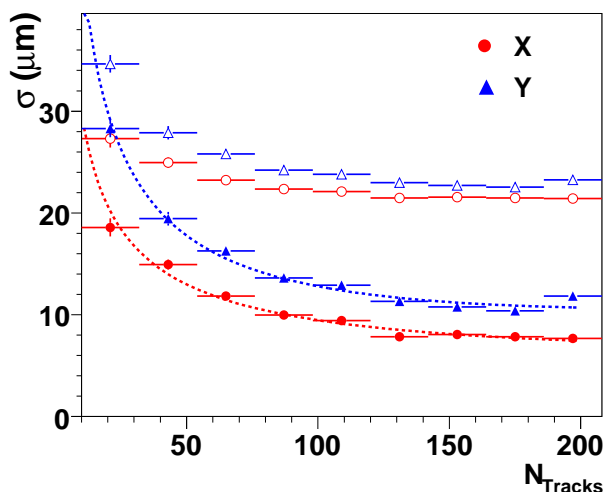


Fig. 3. Dispersion between the transverse coordinates of the interaction vertex given by backtracing the VT tracks and by extrapolating the beam tracker measurement (open symbols), as a function of the number of tracks attached to the vertex. Derived vertex resolution (solid symbols).

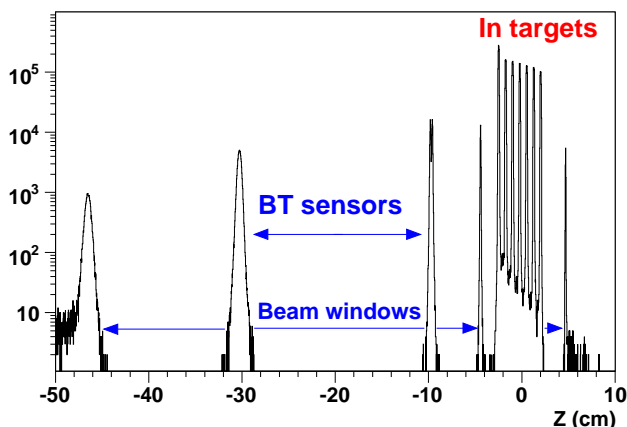


Fig. 4. Distribution of the z coordinate of the interaction vertex for the events that only have one good vertex reconstructed.

evaluated by using the muons from J/ψ decays. Since the $B \rightarrow J/\psi$ contribution is negligible at SPS energies, all the J/ψ mesons are promptly produced. Moreover, the pion and kaon decay background is negligible under the J/ψ peak. Therefore, the offset distribution made with these muons (shown in Fig. 5) directly reflects the resolution of the muon offset measurement: $37 \mu\text{m}$ in x (bending plane) and $45 \mu\text{m}$ in y . These values are the convolution of the track uncertainties with the accuracy of the transverse coordinates of the vertex.

Since the offset resolution of the matched tracks is affected by multiple scattering in the silicon planes, the analysis is performed using a *weighted* muon offset variable, essentially insensitive to the particle's momentum. Its definition is

$$\Delta_{\mu} = \sqrt{\Delta x^2 V_{xx}^{-1} + \Delta y^2 V_{yy}^{-1} + 2\Delta x \Delta y V_{xy}^{-1}} \quad , \quad (1)$$

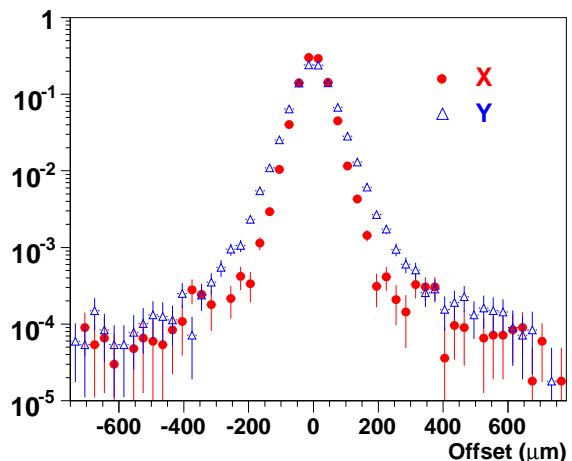


Fig. 5. Offset distribution for matched muons from J/ψ decays, in the x (circles) and y (triangles) coordinates, normalized to unit area.

where V^{-1} is the inverse error matrix accounting for the uncertainties of the vertex fit and of the muon kinematics fit. Δx and Δy are the differences between the coordinates of the vertex and those of the extrapolated muon track, in the transverse plane crossing the beam axis at $z = z_{\text{vertex}}$. We then characterize the dimuon through the *weighted dimuon offset*, defined as

$$\Delta_{\mu\mu} = \sqrt{(\Delta_{\mu 1}^2 + \Delta_{\mu 2}^2)/2} \quad . \quad (2)$$

3 Background subtraction

The sample of collected dimuons include a *combinatorial background* (CB) originating from decays of uncorrelated hadrons, mostly π 's and K 's. Since the production and decay of the parent hadrons are independent processes, this *combinatorial background* (CB) contributes in the same way to the opposite-sign and like-sign samples of muon pairs, increasing quadratically with the charged particle multiplicity. It is important to emphasise that the NA60 trigger treats in exactly the same way the opposite-sign and the like-sign muon pairs.

While this kind of background was already present in previous dimuon experiments, such as NA38 and NA50, a new type of background appears in the NA60 dimuon spectra due to the matching procedure. Indeed, any VT track having a small enough *matching* χ^2 with respect to the muon track is considered a *matching candidate*. For high enough charged particle multiplicities, the muon track will have several possible matches and, naturally, at most one of them is correct. All the other associations are *fake matches* and, if selected, need to be subtracted. Pairs where one muon match is fake and the other one is correct are also part of the *fake matches dimuon background* (FB). Because the probability of having a fake match, for each muon, is proportional to the track density, the yield of matched *muon pairs* where only one muon is fake rises linearly with the charged particle multiplicity, while the yield of doubly fake pairs rises quadratically.

Fig. 6 shows the single muon matching χ^2 distributions for correct and fake matches, normalized to unit area. The distribution for fake matches is obtained from the real data using the *mixed-events technique* (see section 3.2): each muon from the MS is matched with the VT tracks of another event with the same vertex position and multiplicity. Since the probability of having a fake match is determined only by the density of the non-muon tracks in the phase space of the matching parameters, the obtained distribution of the fake matches is automatically obtained with correct normalization. By subtracting it from all matches, the distribution for the correct ones is obtained. One can see that the distribution for the fake matches is much flatter than the corresponding distribution for the correct matches. Selecting exclusively matches with a matching χ^2 below a certain threshold value, the signal-to-background ratio can be improved at the expense of losing some fraction of the signal.

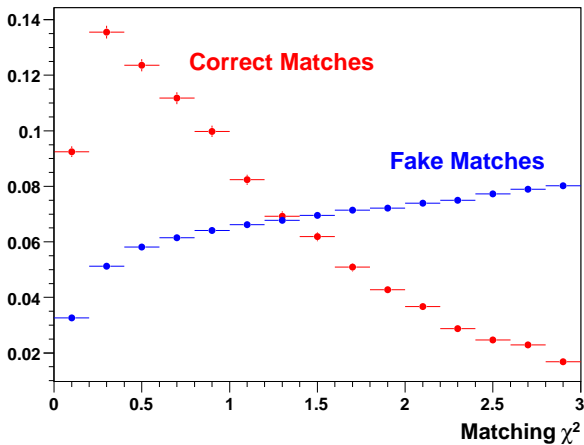


Fig. 6. Matching χ^2 distributions for correct and fake matches, normalized to unit area.

Despite generating the fake matches background, the muon matching procedure leads to a very significant reduction of the combinatorial background due to muons from pion and kaon decays. This happens for two reasons. First, when the pions or kaons decay within the vertex tracker, the kink at the decay point prevents most of the muon tracks from being reconstructed by the silicon tracker, thereby removing these decay muons from the matched muons sample. Second, if the pions or kaons decay downstream of the vertex tracker, the matching between the meson track and the muon track usually results in rather large matching χ^2 values due to the kink between the parent meson and decay muon. By only selecting matches of relatively low χ^2 values, we suppress the yield of *correctly matched* muons from π, K decays.

3.1 Combinatorial background

The combinatorial background contribution to the opposite-sign dimuon distributions can be evaluated from the

measured like-sign muon pair samples, using an *event mixing technique*. Two muons from different events with similar characteristics are randomly picked and paired to build the “mixed CB” sample. Only muon pairs respecting the dimuon trigger conditions are kept (in particular, the muons must be in different sextants). Additionally, a sextant-dependent weight is applied to the measured muons to correct the bias introduced by the “different-sextants” trigger requirement. The mixing is done separately in 40 narrow bins in centrality in order to avoid the bias due to the variation of the single muon kinematics and the μ_+/μ_- ratio within the bin width. The technical details are given in Appendix A. It is important to notice that this mixed-event procedure reproduces not only the shape of the CB spectra but also their absolute normalization.

An important issue to consider in the CB generation concerns the selection of the muons used for the mixing and for the computation of the sextant-dependent weights: they must share the same target, the same field polarities, the same charged track multiplicity bin, and the same configuration of the silicon pixel planes (same acceptances, efficiencies, etc). Since we are interested in determining the background contributions to the *matched* opposite-sign dimuon spectra, it could seem natural to only use for the event mixing single muons which have at least one match. This would ensure that the normalizations, given by Eq. (A-7), would be correctly computed for the matched dimuons spectra. Unfortunately, in the case of the analysis presented in this paper, the event mixing must be made using *all* muons (including non-matched muons), for reasons explained in the next section. Therefore, the computed normalizations correspond to all the dimuons reconstructed in the muon spectrometer, matched and non-matched.

The accuracy of the mixed-event method can be evaluated by comparing the mixed and measured distributions of like-sign muon pairs, as shown in Figs. 7 and 8, respectively for the mass and weighted offset (see also section 3.4 below).

3.2 Fake matches background

The most direct way to evaluate the fake matches background is to use the *overlay Monte Carlo* method: the VT hits of generated dimuons are superimposed on the VT hits of measured data, in order to ensure realistic occupancy conditions. By definition, every matched track built without the sufficient number of the Monte Carlo muon hits is a *fake match* (conventionally we define the match as *fake* if the track has more than two non-muon hits). This method works well for studies that do not use the muon offset information. However, while the kinematic variables of the dimuons are quite robust with respect to the unavoidable differences between the measured and simulated data (in particular the residual misalignment of the geometrical setup), the offset distribution is much more sensitive. Therefore, for studies which require the muon offset information, such as the study reported in this paper, we had to develop a fake subtraction procedure which only

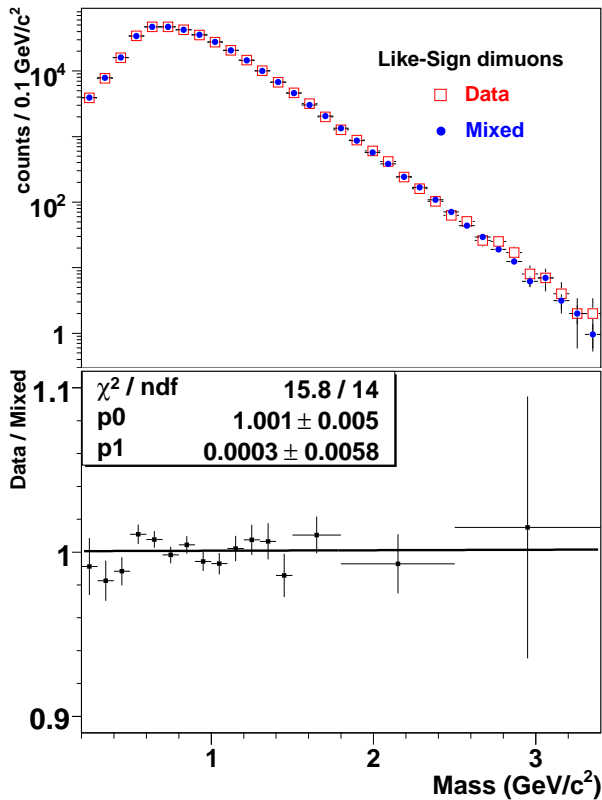


Fig. 7. Measured (squares) and mixed (circles) like-sign dimuon mass spectra (*top*) and their ratio (*bottom*).

uses measured data and provides reliable spectra in any dimuon parameter.

This is again achieved by an *event mixing technique*, matching the muons of a given event with the VT tracks of other events (with the same production target, charged multiplicity, running conditions, etc.), for the real data and for the artificial CB sample. Since the real data sample also contains dimuons where only one of the two muons was incorrectly matched, we added to our simulated FB sample a certain proportion of muon pairs where one of the muons retains its own match (see Appendix B).

In principle, there could be two alternative approaches for reproducing the matched dimuons. If the two muon tracks from the MS have m_1 and m_2 matches, then there are $m_1 \times m_2$ matched dimuons. Given the different shapes of the χ^2 distributions for correct and fake matches (Fig. 6), the pair composed by the two *best matches* (those with the smallest χ^2) has the highest probability of being the correct one. However, this probability decreases with the increase of the number of matching candidates, leading to a degradation of the correct matching efficiency from peripheral to central collisions. Also, as explained in Appendix B, since it appears impossible to estimate analytically the amount of FB in such *best matches* spectra, one should rely on the *overlay Monte Carlo* method. Alternatively, one can consider all $m_1 \times m_2$ matches for a given MS dimuon. Although this will increase the amount of FB to subtract – hence increasing the statistical error – such

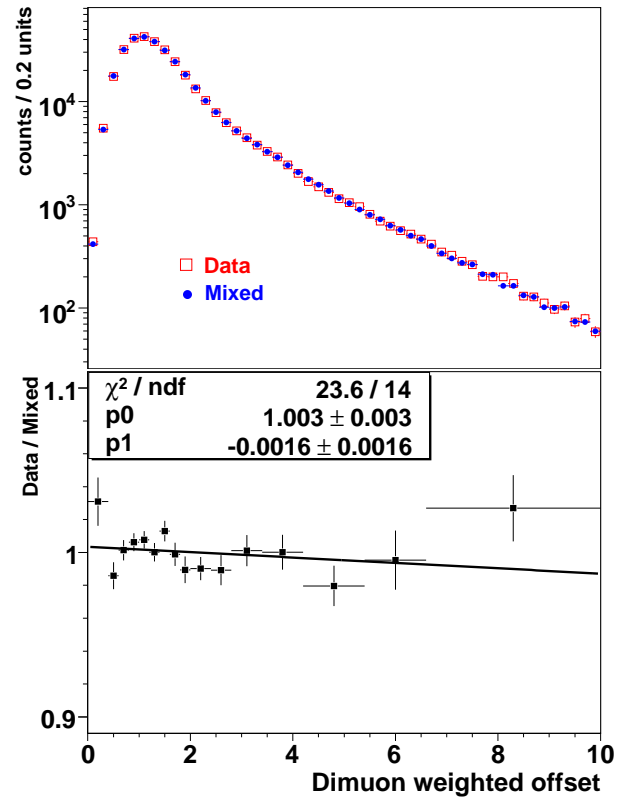


Fig. 8. Same as previous figure but for the dimuon weighted offset.

“*all matches* dimuon spectra” offer a better control of the systematic errors, and allow us to cross-check the Monte Carlo based subtraction method. The results presented in this paper are obtained using this “all matches” procedure. Finally, to reproduce the offsets of the fake matches at the interaction vertex, we apply the same algorithm as used for the CB (see Appendix B).

The top panel of Fig. 9 shows the mass distribution of Monte Carlo ω dimuons (with “all matches”) and those of the fake contributions, both as estimated by Monte Carlo tagging and by event mixing. The bottom panel shows the ratio between the mixed and the MC-tagged fake backgrounds. Both methods are seen to agree in the mass range having meaningful statistics.

3.3 Extraction of the correctly matched signal

The CB and FB contributions obtained via *event mixing* are not independent from each other. As explained above, the combinatorial pairs can be correct or fake matches, $\text{CB} = \text{CB}_{\text{corr}} + \text{CB}_{\text{fake}}$. Clearly, the latter is also present in the total sample of “fake” pairs, due to signal or to combinatorial dimuons, $\text{FB} = \text{FB}_{\text{sig}} + \text{FB}_{\text{cb}}$, with $\text{FB}_{\text{cb}} \equiv \text{CB}_{\text{fake}}$. Therefore, if we subtract the total fake background and the total combinatorial background from the data, we do not obtain the correctly matched signal, because the “fake combinatorial” pairs are subtracted twice: $\text{Data} - \text{FB} - \text{CB} = \text{Data} - \text{FB}_{\text{sig}} - \text{CB}_{\text{corr}} - 2\text{CB}_{\text{fake}} =$

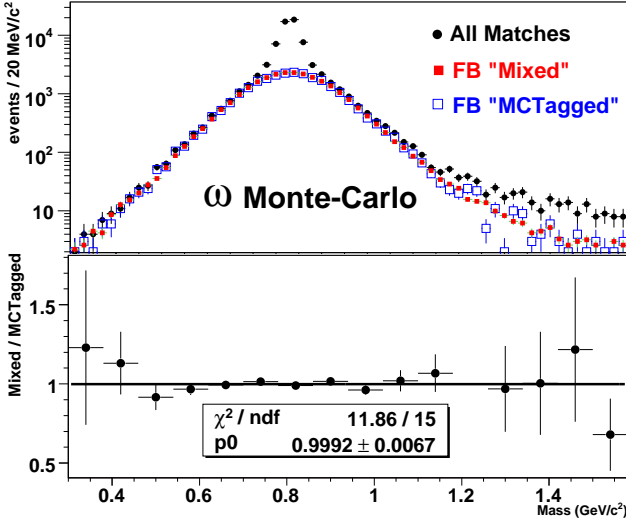


Fig. 9. *Top:* Dimuon mass distributions for the ω simulation, using “all matches” (points), and for the FB, obtained with the *event mixing technique* (filled squares) or by Monte Carlo tagging (open squares). *Bottom:* Ratio between “mixed” and “MC-tagged” fake distributions.

Signal $-$ CB_{fake}. To avoid this double subtraction, we must estimate the “fake combinatorials” contribution. This is done by applying the CB estimation algorithm described in Appendix A to the generated FB sample, using its like-sign pairs for the event mixing.

Figure 10 shows the mass spectra (integrated over all collision centralities) for the measured opposite-sign dimuons, full combinatorial and fake signal background sources, and the extracted correctly matched signal.

Figure 11 shows the *dimuon weighted offsets* distributions. It is worth noticing that the region $2 < \Delta_{\mu\mu} < 6$, de-

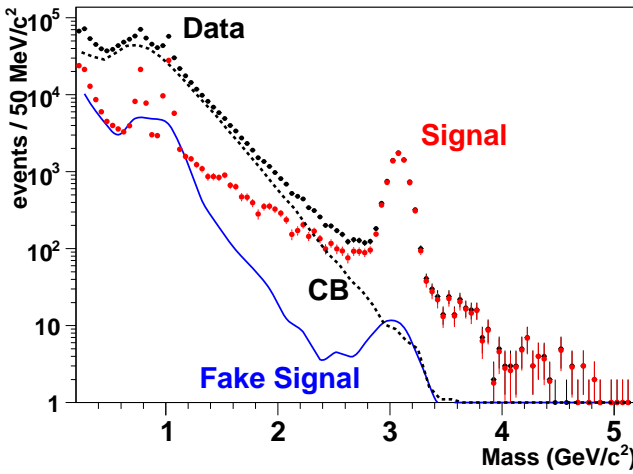


Fig. 10. The measured opposite-sign dimuon mass spectrum (points), the signal (bullets: correctly matched; solid line: incorrectly matched), and the combinatorial background (both correctly and incorrectly matched: dashed line) for the 4000 A data with *matching* $\chi^2 < 1.5$.

cisive to disentangle the open charm contribution from the prompt one, has a significant level of incorrectly matched signal.

3.4 Systematic errors from the background subtraction

The yield of like-sign dimuons remaining after the subtraction of the mixed-event spectra constitutes a very good estimate of the residual combinatorial background contribution left in the opposite-sign spectra. Based on the ratios shown in Fig. 7, 8, the accuracy of the generated background is estimated to be $\sim 1\%$. The resulting systematic uncertainty of the extracted signal is defined by the signal-to-background ratio which strongly depends on the kinematic bin and the cut imposed on the *matching* χ^2 . Being comparable to the statistical error, it changes from $\sim 25\%$ for $p_T < 0.25$ GeV/c at masses around 1.2 GeV/c² to $\sim 1\%$ near 2.5 GeV/c² with a loose cut $\chi^2=3$, and it improves by more than a factor 2 for a $\chi^2=1.5$ cut.

To account for these systematic errors in the several fits mentioned in the next section, whenever necessary, the *statistical* errors of the estimated background were globally scaled up to ensure that the residuals of the like-sign spectra are compatible with zero within three standard deviations. Even in the worst case (when fitting a p_T distribution in a narrow dimuon mass range), the errors were not increased by more than $\sim 10\%$.

The results presented in the next section were checked by repeating the fits with both cuts on the χ^2 and both low and high magnetic field data and were found to be always compatible within the quoted errors.

4 Results

4.1 Expected sources of IMR dimuons

The analysis was separately performed for the 4000 A and 6500 A event samples. Dimuons were selected in the kin-

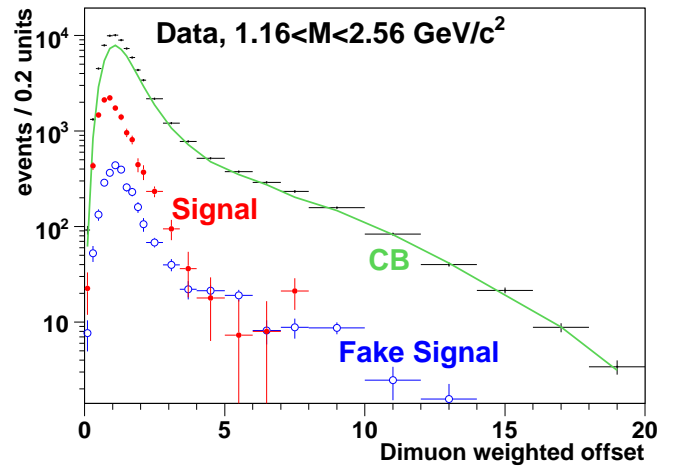


Fig. 11. Data, signal and background spectra for weighted dimuon offset distributions (defined in Eq. 2) in IMR for 4000 A data with *matching* $\chi^2 < 1.5$.

mathematical domain defined by $0 < y_{\text{cms}} < 1$ and $|\cos\theta_{\text{CS}}| < 0.5$, where θ_{CS} is the Collins-Soper decay angle. Only events with a single reconstructed vertex in one of the seven Indium targets were kept for the analysis. Since the signal-to-background ratio strongly depends on the matching χ^2 cut (see Fig. 6), the data were analyzed with two different cuts ($\chi^2 < 1.5$ and $\chi^2 < 3$) to evaluate possible systematic effects related to the background subtraction.

The shapes of the Drell-Yan and open charm contributions were obtained with the Pythia Monte Carlo event generator [19] version 6.325, using the CTEQ6L set of parton distribution functions [20] including nuclear effects through the EKS98 model [21]. The primordial k_{T} was generated from a Gaussian distribution, of width 0.8 GeV/c for Drell-Yan (to describe the p_{T} distribution of dimuons heavier than the J/ψ) and 1.0 GeV/c for the open charm [22]. The charm quark mass was kept at the default value of 1.5 GeV/c² and the P_V parameter (probability that the c -quark hadronizes in vector states) was set to 0.6 [23], resulting in an effective $c\bar{c} \rightarrow \mu^+\mu^-$ branching ratio 0.84%.

The Pythia events were generated at the vertices of real events and propagated through the experimental setup using the Geant 3.2 transport code [24]. The resulting hits were added to those of the real event used to set the interaction vertex and the resulting *overlay Monte Carlo* events were then reconstructed, with the codes used to process the measured data. We only kept the events surviving the selection cuts also applied to the real data. It is worth noticing that the $|\cos\theta_{\text{CS}}| < 0.5$ window significantly cuts the open charm contribution, because Pythia's strong D/ \bar{D} pair correlations give a $\cos\theta_{\text{CS}}$ distribution peaked at -1 and $+1$. This means that the fraction of accepted dimuons from D pair decays is small and very sensitive to the kinematic distributions and correlations used in Pythia. Figure 12 shows the $\cos\theta_{\text{CS}}$ distribution of the $c\bar{c} \rightarrow \mu^+\mu^-$ dimuons, with mass in the range 1.16–2.56 GeV/c², before and after the reconstruction step.

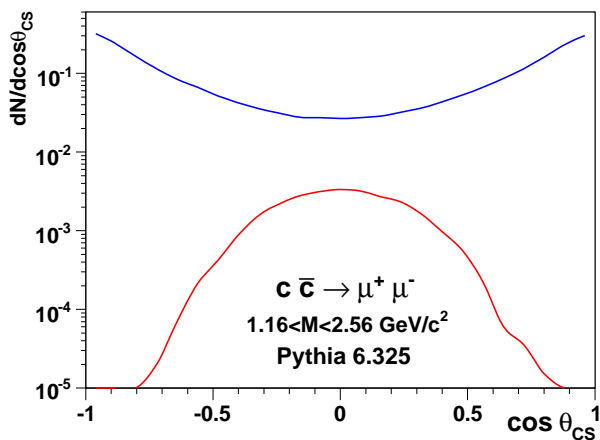


Fig. 12. $\cos\theta_{\text{CS}}$ distribution of $c\bar{c} \rightarrow \mu^+\mu^-$ dimuons in the 1.16–2.56 GeV/c² range, as generated by Pythia, before (upper line, normalized to unit area) and after (lower line) applying the muon reconstruction algorithm.

The basic goal of the analysis is to compare the measured yield of signal IMR dimuons to the *expected* yield, from the Drell-Yan and open charm contributions. Since this comparison is to be done as a function of collision centrality, the events are distributed in 12 sub-samples, using the number of tracks reconstructed in the VT as centrality estimator. The corresponding average number of nucleons participating in the In-In collision, N_{part} , can be derived within the Wounded Nucleon Model $N_{\text{ch}} \approx qN_{\text{part}}$, where N_{ch} is the number of charged particles produced in the VT angular window, corrected for acceptances and efficiencies [25]. The proportionality constant q is found by matching the observed dN/dN_{ch} to dN/dN_{part} generated from the Glauber model.

To judge if the sum of the expected contributions reproduces or not, in amplitude and shape, the measured mass and weighted offset IMR dimuon signal distributions, we must determine the *normalizations* of the Drell-Yan and open charm spectra. We start by fixing the *relative* normalization of the open charm contribution with respect to the Drell-Yan contribution, by calculating the ratio of their production cross sections. In order to calculate this ratio, we use the high-mass Drell-Yan cross sections measured by NA3 [26] and by NA50 [27], which show that Pythia's Drell-Yan spectrum needs to be up-scaled by a K-factor of 1.9, and we use a charm cross section of $\sigma_{c\bar{c}} = 8.6 \mu\text{b}$. The latter number corresponds to the value required to reproduce the dimuon mass distributions measured by NA50 in p-A collisions at 450 GeV [4, 5], $36 \pm 3.5 \mu\text{b}$, scaled down in energy (to 158 GeV) using Pythia. It is worth noting that this value is around 1.8 times higher than what would be obtained from a “world average” estimate [22] based on measurements of D meson production from fully reconstructed hadronic decays. One should stress that neither NA50 nor NA60 are suited to measure the full phase space $c\bar{c}$ cross section: as can be seen from Fig. 12, the acceptance window $|\cos\theta_{\text{CS}}| < 0.5$ defined by the muon spectrometer contains less than 20% of all dimuons from DD decays, and the extrapolation of the measurement to full phase space strongly depends on how well the correlations between the two decay muons are described by Pythia. The obtained open charm to Drell-Yan cross-section ratio is then kept the same for all centrality bins, since both processes are expected to scale with centrality in exactly the same way (proportionally to the number of binary nucleon-nucleon collisions).

The next step is to determine the Drell-Yan normalization from the yield of high-mass dimuons. Given the relatively small statistics, especially when the events are subdivided in several centrality bins, we calculate the Drell-Yan yield from the much larger number of J/ψ events and expected $J/\psi/DY$ ratio. The latter is measured in proton-nucleus collisions [28] by NA50 (at 400–450 GeV and scaled to 158 GeV) and is corrected for the J/ψ “anomalous suppression” measured in In-In collisions [29]. A 10% relative systematic error is applied to the resulting normalizations, to account for uncertainties in the J/ψ anomalous suppression and normal absorption patterns.

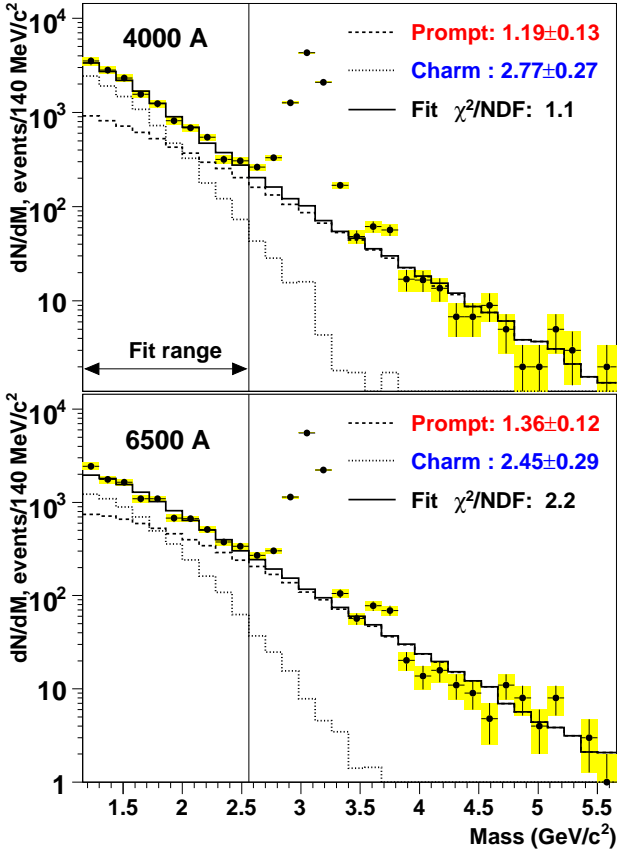


Fig. 13. Signal dimuon mass distribution measured from the 4000 A (*top*) and 6500 A (*bottom*) data samples, compared to the superposition of Drell-Yan dimuons (dashed line) and muon pairs from open charm decays (dotted line), scaled up with respect to the expected yields.

4.2 Data versus expectations in dimuon mass and offset

Figure 13 compares the signal dimuon mass distributions obtained from the 4000 A and 6500 A data samples, integrated over collision centrality, with the sum of the Drell-Yan and open charm contributions. With respect to the expected normalizations, described in the previous paragraphs, these contributions must be scaled up (by the values quoted in the figure) so as to provide the best description of the measured signal spectrum in the dimuon mass window $1.16 < M < 2.56 \text{ GeV}/c^2$. Within errors, the two data samples give perfectly compatible results. A global fit gives scaling factors of 1.26 ± 0.09 for Drell-Yan and 2.61 ± 0.20 for open charm, with $\chi^2/\text{ndf} = 1.02$. Furthermore, essentially the same numerical values are obtained if the analysis is redone only selecting events with a matching χ^2 below 1.5 (instead of 3). As previously observed by NA38 [2] and NA50 [4], a significant *excess* of IMR muon pairs is observed, which can be well accounted for by increasing the charm normalization.

The big advantage of NA60, with respect to the dimuon measurements made by all other heavy-ion experiments, is the availability of the dimuon weighted offset variable,

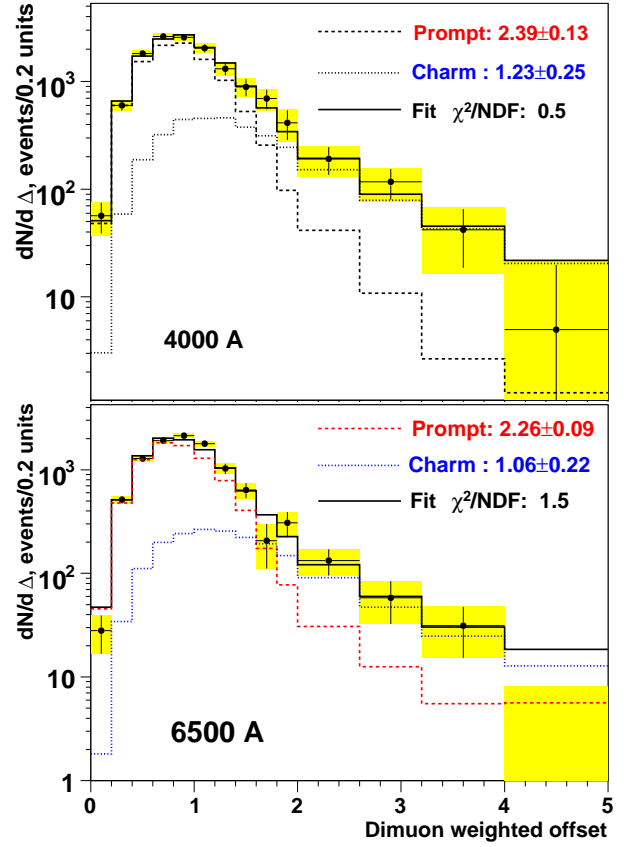


Fig. 14. Same as previous figure but for the dimuon weighted offset distributions of the dimuons in the mass range 1.16–2.56 GeV/c^2 .

which provides complementary information ideally suited to distinguish prompt dimuons from muon pairs stemming from displaced decay vertices. Figure 14 shows the dimuon weighted offset distribution for the signal dimuons in the mass range 1.16–2.56 GeV/c^2 , for the 4000 A and 6500 A data samples, compared to the sum of the two contributions: prompt dimuons and open charm decays, scaled to provide the best fit to data.

The *shape* of the prompt dimuon distribution was built using the measured dimuons in the J/ψ and ϕ peaks, where the non-prompt signal contributions are less than 1%. The shape of the open charm distribution was defined using the muon pairs from the *overlay Monte Carlo* simulation, including the additional smearing needed to reproduce the measured J/ψ and ϕ distributions (see [16], section 8.4.1 for details).

The *excess* dimuons are clearly concentrated in the region of small dimuon offsets, excluding the possibility that they are due to open charm decays. The best description of the measured distribution is obtained when the prompts contribution is scaled up by more than a factor of two with respect to the expected Drell-Yan yield, while the open charm contribution is compatible with the yield assumed by NA50 to reproduce the IMR spectra in p-A collisions [4]. Fig. 14 underlines the fact that the

dimuon weighted offset is a really efficient discriminator between prompt and charm dimuons. On the other hand, due to the extreme similarity of the mass distributions of the *excess* and charm dimuons (see Fig. 16), it is clear that mass alone is completely unable to separate them and, therefore, perfectly accommodates the assumption that the *excess* is due to open charm, from the purely statistical point of view (see Fig. 13).

A global fit of both data sets provides scaling factors of 2.29 ± 0.08 and 1.16 ± 0.16 , for the prompt and open charm contributions, respectively (with $\chi^2/\text{ndf} = 1.52$). If the analysis is redone only using events with matching χ^2 below 1.5, instead of 3, the results remain the same within the statistical errors. If the open charm yield is restricted to be within 10% of the nominal value rather than left free in the fit, the scaling factors become 2.43 ± 0.09 and 1.10 ± 0.10 , respectively, i.e. again the same within the statistical errors.

Since the tail of the offset distribution lacks the statistics needed to define the open charm normalization differentially in bins of mass, p_T and centrality, its scale is kept fixed to the value determined from the integrated sample, corresponding to a full phase space cross section $\sigma_{c\bar{c}} = 9.5 \mu\text{b/nucleon}$ with 14% statistical and 15% systematic errors accounting for the uncertainty of the expected Drell-Yan contribution. This is the value needed to describe the measured data and does not depend on the assumed reference cross section. However, the extrapolation of the cross section to full phase space depends on the kinematical distributions of the simulated c and \bar{c} . The associated uncertainty is not accounted in the quoted systematic error. For instance, we would obtain a value 19% smaller if we would use the conditions of the NA50 analysis: Pythia 5.7, different parton densities and without nuclear modifications, effective $c\bar{c} \rightarrow \mu^+\mu^-$ branching ratio of 0.97% instead of 0.84%, etc.

4.3 Kinematic properties of the excess dimuons

The *excess* dimuons are defined as the statistical difference between the total yield and the sum of fitted charm and nominal Drell-Yan. Unbiased physics insight requires correcting the measured *excess* for reconstruction efficiencies and detection acceptances. The acceptances were calculated by Monte Carlo simulations, in dimuon mass and p_T bins, for each of the two data samples, assuming a uniform $\cos\theta_{CS}$ distribution and the same rapidity distribution as that of the Drell-Yan dimuons (approximately Gaussian with $\sigma \sim 1$). Assuming a Gaussian rapidity distribution of width 1.5 gives 20% less *excess* dimuons, while a 0.5 width leads to 40% more *excess* dimuons. After checking that the 4000 A and 6500 A data sets give statistically compatible results, they were analyzed together. In this way we obtain a two-dimensional distribution of the acceptance-corrected *excess* as a function of mass and p_T .

Figure 15 shows the ratio between the *excess* dimuon yield (corrected for acceptance with the assumptions just mentioned) and the expected Drell-Yan yield (directly taken from the generator), in the mass range 1.16–2.56 GeV/ c^2

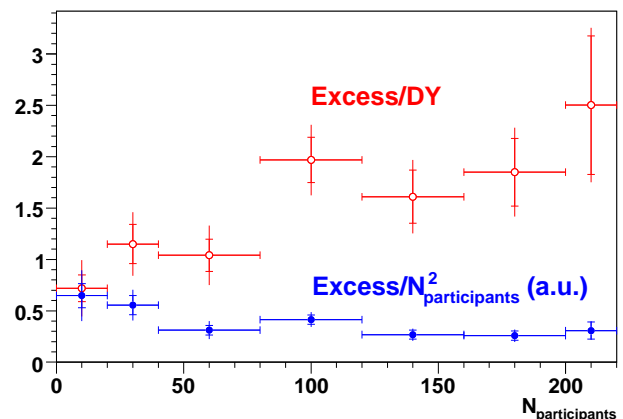


Fig. 15. Ratio between the *excess* and the Drell-Yan dimuon yields, after acceptance correction, versus centrality (open circles). The *excess* per squared number of participants is also shown, in arbitrary units (filled circles).

as a function of N_{part} . The smaller error bars represent the statistical errors while the larger ones represent the sum, in quadrature, of statistical and systematic uncertainties of the fitted Drell-Yan and open charm normalizations. We observe that the yield of *excess* dimuons, per Drell-Yan dimuon, increases from peripheral to central In-In collisions. Furthermore, we see that even the most peripheral event sample has a considerable yield of *excess* dimuons (essentially identical to the yield of expected Drell-Yan dimuons).

To gain further insight into the properties of these *excess* dimuons, we have calculated the ratio between their yield and N_{part}^2 . The *excess*/DY was scaled by the ratio between the number of binary nucleon-nucleon collisions and the squared number of participant nucleons, $N_{\text{coll}}/N_{\text{part}}^2$, calculated for each In-In centrality bin using the Glauber model. The resulting *excess*/ N_{part}^2 ratio, also plotted in Fig. 15, shows a slight decrease with N_{part} . This implies that the increase of the *excess* with centrality is somewhere in between of linear and quadratic in N_{part} .

The mass distribution of the *excess* dimuons, after applying the corrections for acceptance and reconstruction efficiencies, is shown in Fig. 16. The mass spectra of open charm and Drell-Yan pairs are plotted for comparison. The shapes of these spectra are directly taken from the generator. The yields reflect the fit values discussed before; the bands correspond to the associated systematic errors. Clearly, the mass spectrum of the *excess* drops off much more steeply with mass than that of the Drell-Yan pairs. In contrast, the slopes are nearly the same for the *excess* and open charm. This explains why the *excess*, already seen by the NA38/NA50 experiment, was found to be quite fairly described by any source, be it prompt or delayed, with a similar mass distribution as open charm, when using the mass spectrum only as a discriminator [6].

Fig. 17 summarizes the different aspects of the transverse momentum distributions of the *excess* dimuons. The top plot shows the *excess*/DY ratio as a function of the dimuon p_T , clearly indicating that the process responsible

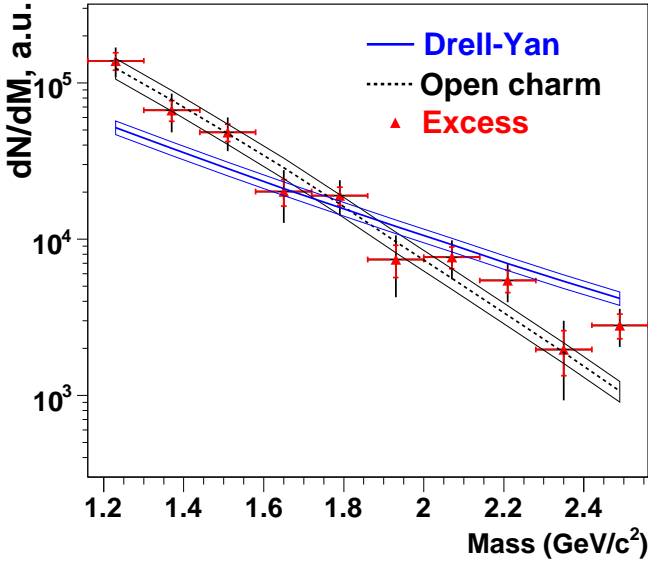


Fig. 16. Mass distribution of all three contributions to the IMR spectrum, corrected for acceptances and efficiencies as described in the text. From top to bottom at the highest mass bin: Drell-Yan (as expected from the measured number of J/ψ dimuons), *excess* (the difference between all prompt and Drell-Yan pairs) and open charm (with scaling factor of 1.16).

for the production of the *excess* dimuons is significantly softer than the Drell-Yan dimuons. While in the lowest p_T bin there are around 3.5 times more *excess* dimuons than expected Drell-Yan dimuons, this ratio drops to 0.5 at high p_T . The p_T spectra themselves are shown in Fig. 17-middle, in 3 consecutive dimuon mass windows: 1.16–1.4, 1.4–2.0 and 2.0–2.56 GeV/c^2 . Again, a significant deviation from the behaviour of Drell-Yan pairs is observed. The three p_T spectra are all different from each other, while the p_T spectra and the mass spectra of Drell-Yan factorize: the primordial $k_T=0.8 \text{ GeV}/c$ characterizing the Gaussian distribution is independent of mass in the region measured, i.e. from 3 to $>10 \text{ GeV}/c^2$ [30].

Finally, Fig. 17-bottom shows the same data in terms of dimuon transverse mass ($m_T = \sqrt{p_T^2 + m^2}$) spectra, for the same three dimuon mass windows defined before. All spectra are essentially exponential. However, a steepening is observed at very low m_T in the lowest mass window, which finds its counterpart in all m_T spectra observed in the low mass region below $1 \text{ GeV}/c^2$ [31], but seems to be switched-off in the upper two mass windows as seen here. The phenomenon is outside any systematic errors as discussed in [31], but has so far not found a convincing physical interpretation. Ignoring the low- m_T rise, the data can be fit with simple exponentials $1/p_T dN/dp_T = 1/m_T dN/dm_T \sim \exp(-m_T/T)$ over the complete p_T -range (lines in Fig. 17-middle and bottom), resulting in the following respective T_{eff} values: 189 ± 15 (*stat*) ± 4 (*syst*), $197 \pm 13 \pm 2$, and $166 \pm 17 \pm 4 \text{ MeV}$. The systematic errors are dominated by the uncertainties of the Drell-Yan and open charm contributions. If the fit is instead restricted to $p_T \geq 0.5 \text{ GeV}/c$, consistent with [31] to exclude the rise at low- m_T , the T_{eff} values slightly (but hardly significantly)

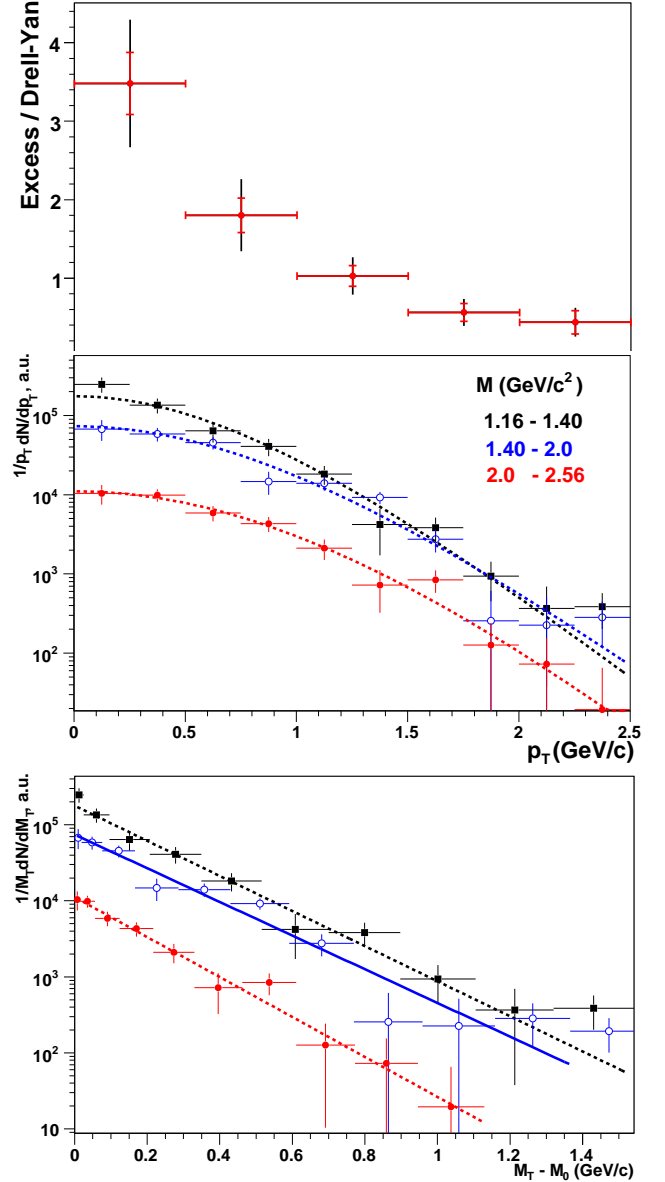


Fig. 17. Ratio between the *excess* and the Drell-Yan dimuon yields, after acceptance correction, versus dimuon transverse momentum (*top*). Transverse momentum (*middle*) and transverse mass (*bottom*) spectra of the *excess* dimuons, in three dimuon mass windows: 1.16–1.4, 1.4–2.0 and 2.0–2.56 GeV/c^2 .

rise to $199 \pm 21 \pm 3$, $193 \pm 16 \pm 2$ and $171 \pm 21 \pm 3 \text{ MeV}$, respectively.

5 Discussion

The central results of the present paper are connected to two essentially independent physics issues:

- The observed yield of muon pairs from D meson decays leads to $\sigma_{c\bar{c}} = 9.5 \pm 1.3(\text{stat}) \pm 1.4(\text{syst}) \mu\text{b}$ (the systematic error does not reflect the uncertainty related to the kinematic distribution of the c and \bar{c} quarks)

and is compatible with the charm production cross section deduced from the IMR dimuon data measured by NA50 in p-A collisions. Charm production in A-A collisions is *not enhanced* relative to expectations, and it therefore cannot be made responsible for the dimuon enhancement seen by NA38 and NA50.

- The dimuon enhancement in the IMR as observed before in Pb-Pb collisions also exists in In-In collisions. It is now experimentally proven to be solely due to the *prompt* component. The dimuon *excess* has been statistically isolated by subtracting the Drell-Yan and open charm contributions from the total. It is on about the same level as Drell-Yan (and charm) and increases significantly from peripheral to central collisions relative to Drell-Yan and N_{part} . Both its mass and p_T spectra show a much steeper fall-off than Drell-Yan. Moreover, the p_T spectra depend on mass and do not show the factorization between mass and p_T characteristic for Drell-Yan. Conversely, fits to the essentially exponential m_T -spectra lead to inverse slope parameters T_{eff} , of about 190 MeV, which do not depend on mass, within the (relatively large) errors.

The prime contender for the interpretation of the *excess* is *thermal radiation*. The remainder of this section places the results reported in this paper into a wider context, relating them to other experimental results from NA60 and to the latest theoretical predictions on thermal radiation in the IMR.

NA60 has also studied dimuon mass and p_T spectra in the low mass region (LMR) $M < 1 \text{ GeV}/c^2$ [31,32,33]. The total mass spectrum, unifying the results from the LMR analysis and from the IMR data in Fig. 16, is shown in Fig. 18-top. The LMR results correspond to the integral of the p_T -differential acceptance-corrected mass spectra published previously [32,33]; a cut $p_T > 0.2 \text{ GeV}/c$ is applied to avoid the very large errors in the region of low acceptance [32,33]. The mass spectrum is absolutely normalized in the LMR region as described in [32]; the IMR data from Fig. 16 have independently been normalized following an analogous procedure. Recent theoretical results on thermal radiation from two major groups working in the field are included for comparison [34,35], calculated absolutely (not normalized relative to the data); a further result [36] exists, but is left out here due to the lack of final normalization. The general agreement between data and model results both as to spectral shapes and to absolute yields is most remarkable, supporting the term "thermal" used throughout this paper. The strong rise towards low masses reflects the Boltzmann factor, i.e. the Planck-like radiation associated with a very broad, nearly flat spectral function. Even this part is well described by [34], due to the particularly large contribution from baryonic interactions to the low-mass tail of the ρ spectral function in this model. Higher up in mass, the ρ pole remains visible, followed by a broad bump in the region of the ϕ . This is described in [34] as in-medium broadening of a small fraction of the ϕ (caution should, however, be presently taken on that, since corrections for the resolution function of the NA60 apparatus are still under investigation). In the IMR

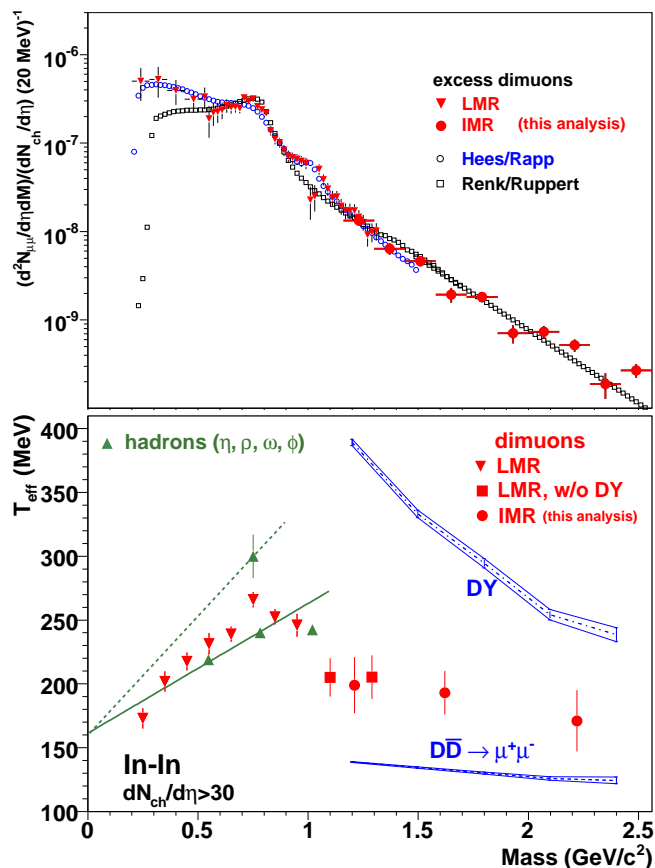


Fig. 18. *Top:* Acceptance-corrected mass spectra of the excess dimuons for the combined LMR/IMR. Errors in the LMR part are statistical; the systematic errors are mostly smaller than that. Errors in the IMR part are total errors. The theoretical model results are labeled according to the authors Hees/Rapp [34] (EoS-B⁺ option is used) and Renk/Ruppert [35]. *Bottom:* Inverse slope parameter T_{eff} of the *excess* m_T -spectra vs. dimuon mass [31,32]. For the LMR data $M < 1 \text{ GeV}/c^2$ (triangles), Drell-Yan is not subtracted (would decrease the values only within the error bars [31]). The IMR data (closed circles) correspond to the present work. Open charm is subtracted throughout. The bands show the inverse slopes for the Drell-Yan and open charm contributions as provided by Pythia.

region above $1 \text{ GeV}/c^2$, the description is good for both scenarios (only available up to $1.5 \text{ GeV}/c^2$ for [34]).

Both for the LMR and IMR, the m_T -spectra are pure exponentials (at least for $p_T > 0.4 \text{ GeV}/c$), consistent with the thermal interpretation [35,36]. Apart from the absolute scale, they can therefore be described by one single parameter, the inverse slope T_{eff} extracted from exponential fits to the data. The combined results for T_{eff} in the LMR and those reported in this paper are shown in Fig. 18-bottom [31]. For $M < 1 \text{ GeV}/c^2$ (triangles), a correction for Drell-Yan pairs is not done, due to their small contribution [31], the intrinsic uncertainties at low masses [34] as well as the inability of Pythia to generate Drell-Yan in this region. The square points correspond to the exten-

sion of the LMR analysis up to $M = 1.4 \text{ GeV}/c^2$ which did not account for the systematic errors of the Drell-Yan and open charm contributions. One should note that the square points and circles are not statistically independent, since the two analyses were performed on overlapping data samples. The inverse slopes for the Drell-Yan and open charm contributions are shown for comparison. The difference to the excess data is most remarkable.

Below $1 \text{ GeV}/c^2$, the inverse slope parameters T_{eff} are not at all independent of dimuon mass, but monotonically rise with mass from the dimuon threshold, where T_{eff} is $\sim 180 \text{ MeV}$, up to the nominal pole of the ρ meson, where T_{eff} is $\sim 250 \text{ MeV}$. This is followed by a sudden decline to the level of $T_{\text{eff}} \sim 190 \text{ MeV}$ reported here. That decline becomes even more steep, jump-like, if the slope parameters T_{eff} are corrected for the contribution of the freeze-out ρ [33]. The initial rise is consistent with the expectations for radial flow of a *hadronic* source (here $\pi^+\pi^- \rightarrow \rho$) decaying into lepton pairs. However, extrapolating the lower-mass trend to beyond $1 \text{ GeV}/c^2$, a jump of about 50 MeV down to a low-flow situation is extremely hard to reconcile with emission sources which continue to be of dominantly hadronic origin in this region. Rather, the sudden loss of flow is most naturally explained as a transition to a qualitatively different source, implying dominantly early, i.e. *partonic* processes like $q\bar{q} \rightarrow \mu^+\mu^-$ for which flow has not yet built up, at least at SPS energies, due to the "soft point" in the equation-of-state. This may well represent the first direct, i.e. data-based evidence for thermal radiation of partonic origin, overcoming parton-hadron duality for the *yield* description in the mass domain (see below). The observed slope parameters $T_{\text{eff}} \sim 190 \text{ MeV}$ are then perfectly reasonable, with a purely *thermal* interpretation without much flow, reflecting the averaging in the space-time evolution of the fireball between the initial temperature $T_i \sim 220\text{-}250 \text{ MeV}$ (at the SPS) and the critical temperature $T_c \sim 170 \text{ MeV}$.

Theoretically, the NA50 IMR dimuon enhancement [6] was successfully described as thermal radiation based on parton-hadron duality, without specifying the individual sources [7]. However, the same approach is not any longer appropriate for the NA60 data. The extension of the unified LMR and IMR results over the complete M - p_T plane places severe constraints on the dynamical trajectories of the fireball evolution, allowing for more detailed insight into the origin of the different dilepton sources on the basis of radial flow, sensitive to the time ordering of the sources. Indeed, all present scenarios [34, 35, 36] explicitly differentiate between hadronic (mostly 4π) and partonic contributions in the IMR. The partonic fraction ranges from 0.65 for [34] (option EoS-B⁺ as used in Fig. 18-top) to "dominant" in [35, 36]. However, due to remaining uncertainties in the equation-of-state, in the fireball evolution and in the role of hard processes [34], a quantitative description of the very sensitive inverse slope parameter T_{eff} in Fig. 18-bottom is only slowly emerging. In particular, the more recent results from the authors of [35, 36], while very encouraging, are still preliminary and have not yet been formally published in their final form. A system-

atic comparison of several model results to the data in Fig. 18-bottom is therefore presently not possible.

6 Conclusions

The dimuon *excess* in the mass region $M > 1 \text{ GeV}/c^2$ seen in high-energy nuclear collisions before has now been proven to be of prompt origin. Its properties, differing from those of Drell-Yan pairs in many ways, suggest an interpretation as thermal radiation. If linked to supplementary information on dimuon *excess* production in the mass region $< 1 \text{ GeV}/c^2$, all indications favor an early, i.e. a dominantly partonic emission source. Present theoretical modelling, though still under development, supports our interpretation.

7 Acknowledgments

This work was partially supported by the Fundação para a Ciência e a Tecnologia (Portugal), under the SFRH/BPD/5656/2001 and POCTI/FP/FNU/50173/2003 contracts, by the Gulbenkian Foundation (Portugal) and by the Fund Kidagan (Switzerland).

Appendix A : Combinatorial background

Our aim is to pick pairs of muons from different events in such a way that after applying the trigger conditions they reproduce the observed like-sign spectra, both in shape and in absolute normalization. The problem arises from the fact that the data used as pool for the single muon sample is already affected by the trigger conditions which induces correlations between the registered muons. We will now describe the procedure used to account for these correlations and to obtain the "unbiased" single muon pools.

We will denote by P^+ and P^- the average numbers of triggerable muons of positive and negative charge, respectively, in a single interaction (the numerical values of these probabilities are always $\ll 1$ since the probability for pion to produce a triggerable muon is $\sim 10^{-3}$). If we neglect the correlation induced by charge conservation between the numbers of positive and negative hadrons (a very reasonable assumption in the case of high multiplicity heavy-ion collisions), the number of muon pairs of different charge combinations observed in N collisions will be

$$\begin{aligned} N^{++} &= NP^{++} = NP^+P^+/2 \\ N^{--} &= NP^{--} = NP^-P^-/2 \\ N^{+-} &= NP^{+-} = NP^+P^- \end{aligned} \quad (\text{A-1})$$

To account for the rejection of the same-sextant muon pairs by the trigger, we decompose P^+ (and P^-) in the contributions from the different sextants, $P^+ = \sum_{i=1}^6 p_i^+$,

and rewrite Eqs. (A-1) excluding the rejected combination:

$$\begin{aligned}\hat{P}^{++} &= \sum_{i<j}^6 p_i^+ p_j^+ = \left(P^+ P^+ - \sum_i^6 p_i^{+2} \right) / 2 \\ \hat{P}^{--} &= \sum_{i<j}^6 p_i^- p_j^- = \left(P^- P^- - \sum_i^6 p_i^{-2} \right) / 2 \\ \hat{P}^{+-} &= \sum_{i \neq j}^6 p_i^+ p_j^- = P^+ P^- - \sum_i^6 p_i^+ p_i^- .\end{aligned}\quad (\text{A-2})$$

It is worth noting that Eqs. (A-2) imply:

$$\begin{aligned}\left(\hat{P}^{+-} \right)^2 - 4 \hat{P}^{++} \hat{P}^{--} &= \sum_i^6 \left(P^+ p_i^- - P^- p_i^+ \right)^2 - \\ &\sum_{i \neq j}^6 p_i^+ p_j^- \left(p_i^+ p_j^- - p_j^+ p_i^- \right)\end{aligned}\quad (\text{A-3})$$

The well-known equation $N^{+-} = 2\sqrt{N^{++}N^{--}}$ is a particular case of Eq. (A-3) when its right-hand side vanishes. Rewriting the latter as

$$\begin{aligned}\sum_i^6 \left[\sum_j^6 p_j^+ p_i^- \left(1 - \frac{p_i^+}{p_i^-} / \frac{p_j^+}{p_j^-} \right) \right]^2 \\ - \sum_{i \neq j}^6 p_i^{+2} p_j^{-2} \left(1 - \frac{p_j^+}{p_j^-} / \frac{p_i^+}{p_i^-} \right) ,\end{aligned}\quad (\text{A-4})$$

we see that it vanishes when the p_i^+/p_i^- ratios are the same for all sextants (in more general terms, this ratio should be constant over the whole phase space). This is not the case in NA60 because the dipole magnet breaks the symmetry of the azimuthal distribution of the produced particles, in a charge dependent way. Therefore, in order to evaluate the **CB** in NA60, we need to compute the single muon probabilities and explicitly account for the exclusion of the same-sextant dimuons. Since the number of same-sign pairs with muons in the sextants i and j is, for the positive case, $N_{ij}^+ = \rho_i^+ \rho_j^+ / 2$, with $\rho_i^+ = \sqrt{N} p_i^+$, we can extract ρ_i^+ as

$$\left(\rho_i^+ \right)^2 = \frac{N_{ij}^+ N_{ik}^+}{N_{jk}^+} \quad (\text{A-5})$$

and then average over all possible $\{j, k\}$ combinations. Once the values of ρ_i^+ and ρ_i^- are known, we can determine the fractions of positive and of negative muons, no longer being biased by the trigger condition:

$$R^+ = \frac{\sum \rho_i^+}{\sum \rho_i^+ + \sum \rho_i^-} , \quad R^- = 1 - R^+ . \quad (\text{A-6})$$

We can, then, build the artificial **CB** spectra according to the following procedure:

- i. Select randomly the charges of the two muons, according to the probabilities given by Eqs. (A-6).

- ii. Select randomly the sextant of each muon, according to the weights ρ_i^+ and ρ_i^- , restarting from step 1 if the two selected sextants happen to be the same.
- iii. Randomly pick two muons, of charges and sextants as previously selected, from the single muon samples built out of the measured like-sign dimuon events. If the two selected muons have more than one match to VT tracks (m_1 and m_2 matches, say), then we build all possible ($m_1 \times m_2$) matched *dimuons* and apply to each of them the selection cuts applied to the measured events.

The normalizations of these artificial **CB** samples are fixed by

$$N^{+-} = \sum_{i \neq j} \rho_i^+ \rho_j^- , \quad N^{++(---)} = \frac{1}{2} \sum_{i \neq j} \rho_i^{+(-)} \rho_j^{+(-)} , \quad (\text{A-7})$$

so that the generated like-sign dimuon spectra reproduce the corresponding measured spectra.

Special care must be taken in what concerns the *offsets* of the muons in the ‘‘mixed’’ pairs. In order to reproduce the offset distribution of the measured combinatorial muons, we first randomly assign the vertex of one of the two events participating in the mixing to be the vertex of the generated event. Then, we modify the intercept parameters of the muon from the other event so that with respect to this vertex it retains the same offset as it had in its own event, with respect to its vertex. The accuracy of the method schematically depicted in Fig. 19 can be appreciated in Fig. 8, which compares the *dimuon weighted offset* distributions of the generated and measured like-sign muon pairs.

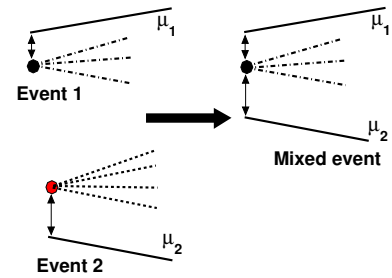


Fig. 19. Schematic explanation of the method used to build the muon offsets for mixed events.

Appendix B : Fake matches background

Our aim is to estimate the probability for a given muon from the MS to be wrongly matched with the tracks in the VT and to use it in building the artificial *fake dimuons*

sample which reproduces both in spectral shape and in normalization the **FB** contributing to data.

Let ϵ be the probability that the correct match is present in the set of all found matches for a muon with given kinematics (regardless on the number of fake matches and their matching χ^2 's). Notice that the correct match may be missing not only due to track reconstruction inefficiency or the choice of the χ^2 cut value, but also because the muon was produced in a decay or interaction downstream of the VT, in which case its track is simply absent. Let us denote by ϕ_n ($n \geq 0$) the probability for a given muon to have n fake matches in events with given characteristics such as interaction sub-target, multiplicity, etc. If we designate ν as the average number of fake matches, then ϕ_n is Poisson distributed with mean ν . Our derivations do not require, however, any assumption about its distribution.

These quantities can be extracted for each muon with arbitrary precision using a *event mixing technique* in the following way: one applies the usual matching procedure but tries to associate the MS muon of one event with the VT tracks of many different events with same characteristics (i.e. multiplicity, interaction sub-target, etc.). From each such event one gets a set of *a priori* fake matches with the same ϕ_n and χ^2 distributions as for the fakes in the real data. The latter distribution, $B(\chi^2)$ (scaled down by the number of tried events per muon), after being subtracted from the χ^2 distribution of the real data, provides the spectrum for the correct matches, $S(\chi^2)$ (both $B(\chi^2)$ and $S(\chi^2)$ are shown in Fig. 6). Then, the probability for a given muon to have n matches (either one correct and $n-1$ fakes or all n fakes) can be written as:

$$P(n) = \epsilon\phi_{n-1} + (1-\epsilon)\phi_n \quad (\text{B-1})$$

and the probability that the correct match is present in this n -plet is

$$P_{pr}(n) = \epsilon\phi_{n-1}/P(n) \quad (\text{B-2})$$

Provided that the correct match is present in this set of n matches, Bayes' theorem states that the fraction of times $W_b(n|pr)$ in which it will have the smallest (*best*) χ^2 is equal to the ratio of the probability for configuration $\{\chi_{1,corr}^2, \dots\}$ to the sum of probabilities for all configurations with given χ^2 values (i.e. $\{\chi_{1,fake}^2, \chi_{2,corr}^2, \dots\}$, etc.). Expressing the probability of given arrangement of χ^2 values of n matches as the product of the probabilities for each χ^2 , we can write:

$$W_b(n|pr) = \frac{S(\chi_1^2) \prod_{j=2}^n B(\chi_j^2)}{\sum_{i=1}^n S(\chi_i^2) \prod_{j \neq i}^n B(\chi_j^2)} = \frac{R_1}{\sum_{i=1}^n R_i} \quad (\text{B-3})$$

with $R_i = S(\chi_i^2)/B(\chi_i^2)$. From Eqs. (B-1–B-3) we get the probability for the *best* one of n matches being the correct one:

$$W_b(n) = P_{pr}(n)W_b(n|pr) = \frac{\epsilon R_1}{\left(1 + \frac{1-\epsilon}{\epsilon} \frac{\phi_n}{\phi_{n-1}}\right) \sum_{i=1}^n R_i} \quad (\text{B-4})$$

It is the presence of the ϵ in Eq. (B-4) which makes it difficult to estimate the **FB** in the *best matches* spectra using the data only: the probability of the correct match being present in the set of the matches strongly depends on the kinematics of the muon. Even for muons with similar kinematics it differs for those coming from the interaction point and those originating in π or K decays.

Consider now a pair of muons, each with its own ϵ_i and $\phi_n^{(i)}$, $i = 1, 2$. For the sake of generality consider two extreme possibilities: the case in which the probability of finding the correct match for the first muon is not correlated with that of the second muon and the case in which the correct matches are present or absent always together, with common probability ϵ . In the first case the probability of finding n and k matches respectively, similarly to Eq. (B-1), can be written as:

$$P(n, k) = \left[\epsilon_1 \phi_{n-1}^{(1)} + (1-\epsilon_1) \phi_n^{(1)} \right] \left[\epsilon_2 \phi_{k-1}^{(2)} + (1-\epsilon_2) \phi_k^{(2)} \right] \quad (\text{B-5})$$

while in the second, full correlation, case we have

$$P(n, k) = \epsilon \phi_{n-1}^{(1)} \phi_{k-1}^{(2)} + (1-\epsilon) \phi_n^{(1)} \phi_k^{(2)} \quad (\text{B-6})$$

Taking into account the identities $\sum_1^\infty n \phi_{n-1} = \nu + 1$, $\sum_0^\infty n \phi_n = \nu$ and $\sum_0^\infty \phi_n = 1$, the average number of matched dimuons for given pair, $W = \sum_{n,k=1}^\infty nkP(n, k)$, is equal to

$$W = \epsilon_1 \epsilon_2 + [\epsilon_1 \nu_2 + \epsilon_2 \nu_1 + \nu_1 \nu_2] \quad (\text{B-7})$$

for the case of absence of the correlation between the correct matches and

$$W = \epsilon + [\epsilon(\nu_1 + \nu_2) + \nu_1 \nu_2] \quad (\text{B-8})$$

for the correlated case. Note that in Eqs. (B-7–B-8) the expression in square brackets (involving the average number of fake matches per muon, ν) gives the average number of fake dimuons which is what we want to reproduce by the *event mixing technique*.

We thus arrive at the following procedure for a given pair of muons from the MS (including those which have no matches)

- i. For each muon of the pair we generate the “mixed fakes” by selecting matches from the same number of tracks as in the event where the pair comes from, but picking the tracks from other events with similar characteristics.
- ii. Combine all mixed fakes of the first muon with all original matches (if any) of the second one and vice-versa. The probability of obtaining this way $n \times k$ (including the cases of n or $k = 0$) *a priori* fake dimuons is

$$F(n, k) = \phi_n^{(1)} \sum_{l=0}^\infty P(l, k) + \phi_k^{(2)} \sum_{l=0}^\infty P(n, l) \quad (\text{B-9})$$

which, after substitution of Eq. (B-6), leads to

$$F(n, k) = \phi_n^{(1)} \left[\epsilon \phi_{k-1}^{(2)} + (1-\epsilon) \phi_k^{(2)} \right] + \phi_k^{(2)} \left[\epsilon \phi_{n-1}^{(1)} + (1-\epsilon) \phi_n^{(1)} \right] \quad (\text{B-10})$$

in the uncorrelated scenario and

$$F(n, k) = \epsilon \left[\phi_n^{(1)} \phi_{k-1}^{(2)} + \phi_{n-1}^{(1)} \phi_k^{(2)} \right] \quad (\text{B-11})$$

for the correlated one. Averaging over all possible $\{n, k\}$ combinations (i.e. performing these two steps many times with different events using the same muon pair) we get for the average number of “mixed fake dimuons”, W_1 , defined as $\sum_{n,k=1}^{\infty} nkF(n, k)$,

$$W_1 = \epsilon_1 \nu_2 + \epsilon_2 \nu_1 + 2\nu_1 \nu_2 \quad , \quad (\text{B-12})$$

$$W_1 = \epsilon(\nu_1 + \nu_2) + 2\nu_1 \nu_2 \quad , \quad (\text{B-13})$$

for the uncorrelated and correlated cases, respectively.

Note that these numbers reproduce the fake dimuons contribution (in []) of Eqs. (B-7) and (B-8), respectively, except for an extra factor 2 in the term corresponding to both matches being fake. This double counting can be easily removed by combining the mixed fake matches of the first muon with those of the second one and counting these dimuons with a negative sign, thus obtaining the needed $W_2 = -\nu_1 \nu_2$ contribution.

This algorithm does not require any explicit determination of ϵ 's of ϕ_n 's. For each pair of muons large amounts of “mixed” fake dimuons are generated with small weights $(W_1 - W_2)/N$, where N is the number of different events matched to the same muon pair, thus smoothing the bin to bin fluctuations.

References

1. E.V. Shuryak, Phys. Rep. **61** (1980) 71.
J. Kapusta, P. Lichard and D. Seibert, Phys. Rev. **D44** (1991) 2774.
P.V. Ruuskanen, Nucl. Phys. **A544** (1992) 169c.
G.Q. Li and C. Gale, Phys. Rev. Lett. **81** (1998) 1572.
2. C. Lourenço *et al.* (NA38 Coll.), Nucl. Phys. **A566** (1994) 77c.
3. A.L.S. Angelis *et al.* (HELIOS-3 Coll.), Eur. Phys. J. **C13** (2000) 433.
4. M.C. Abreu *et al.* (NA50 Coll.), Eur. Phys. J. **C14** (2000) 443.
5. C. Soave, Tesi di Dottorato di Ricerca, Universita degli studi di Torino, April 1998.
6. L.Capelli *et al.* (NA38/NA50 Coll.), Nucl. Phys. **A698** (2002) 539c.
7. R. Rapp and E. Shuryak, Phys. Lett. **B473** (2000) 13.
8. P. Lévai, B. Müller and X.-N. Wang, Phys. Rev. **C51** (1995) 3326.
9. Z. Lin and X.-N. Wang, Phys. Lett. **B444** (1998) 245.
10. J.W. Qiu and X.F. Zhang, Phys. Lett. **B525** (2002) 265.
11. C. Spieles *et al.*, Eur. Phys. J. **C5** (1998) 349.
12. R.Shahoyan, proceedings of Quark Matter 2006, Phys. **G34** (2007) 1029.
13. M.C. Abreu *et al.* (NA50 Coll.), Phys. Lett. **B410** (1997) 327.
14. M. Keil *et al.*, Nucl. Instrum. Meth. **A549** (2005) 20.
15. S.Damjanovic *et al.* (NA60 Coll.), Eur.Phys.J **C49** (2007) 235 and Nucl.Phys **A783** (2007) 327.
16. A.David, PhD thesis, Instituto Superior Técnico, Universidade Técnica de Lisboa, 2005, (CERN-THESIS-2006-007).
17. K. Wyllie *et al.*, Proc. of the Fifth Workshop on Electronics for LHC Experiments, Snowmass, Colorado (1999).
18. L. Casagrande *et al.*, Nucl. Instrum. Meth. **A478** (2002) 325.
19. T. Sjöstrand *et al.*, Computer Phys. Comm. **135** (2001) 238.
20. J. Pumplin *et al.*, J. High Energy Phys. **07** (2002) 012.
21. K.J. Eskola, V.J. Kolhinen and C.A. Salgado, Eur. Phys. J. **C9** (1999) 61.
22. H.K. Wöhri and C. Lourenço, J. Phys. **G30** (2004) S315; C. Lourenço and H.K. Wöhri, Phys. Rep. **433** (2006) 127.
23. A. David, Phys. Lett. **B644** (2007) 224.
24. GEANT, <http://wwasd.web.cern.ch/wwasd/geant>
25. M. Floris *et al.* NA60 Coll., Phys.Conf.Ser.5:55-63,2005.
26. J. Badier *et al.* (NA3 Coll.), Z. Phys. **C26** (1985) 489.
27. M.C. Abreu *et al.* (NA50 Coll.), Phys. Lett. **B410** (1997) 337.
28. B. Alessandro *et al.* (NA50 Coll.), Eur. Phys. J **C39** (2007) 335.
29. R. Arnaldi *et al.* (NA60 Coll.), Phys. Rev. Lett. **99** (2007) 132302.
30. G. Moreno *et al.* Phys.Rev. **D43** (1991) 2815.
31. R. Arnaldi *et al.* (NA60 Coll.), Phys. Rev. Lett. **100** (2008) 022302
32. S. Damjanovic *et al.* (NA60 Coll.), J. Phys. G. **35** (2008) 104036; nucl-ex/0805.4153/.
33. S. Damjanovic *et al.* (NA60 Coll.), nucl-ex/812.3053/.
34. H. van Hees and R. Rapp, Nucl.Phys. **A806** (2008) 339.
35. J. Ruppert, C. Gale, T. Renk, P. Litchard and J. Kapusta, Phys.Rev.Lett. **100** (2008) 162301; T. Renk and J. Ruppert, Phys.Rev. **C77** (2008) 024907.
36. K. Dusling, D. Teaney and I. Zahed, Phys.Rev. **C75** (2007) 024908; hep-ph/0701253/